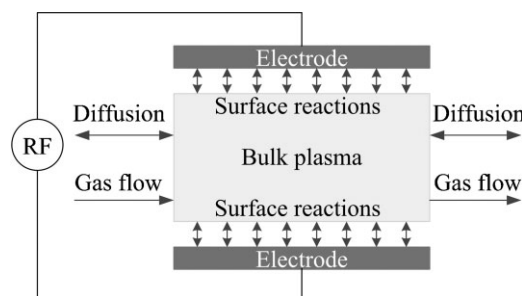


Main Species and Physicochemical Processes in Cold Atmospheric-pressure He + O₂ Plasmas

Ding-Xin Liu, Ming-Zhe Rong, Xiao-Hua Wang, Felipe Iza,* Michael G. Kong, Peter Bruggeman

The main species and chemical processes in low-temperature atmospheric-pressure He + O₂ plasmas are identified using a comprehensive global model. The simulation results highlight the significance of Penning processes at low oxygen concentration, and the increasingly important role of electron attachment as the oxygen concentration increases. With increasing the oxygen concentration, the electron energy dissipation shifts from elastic collisions with He to dissociative excitation and attachment of O₂ molecules, and large ions (O₃⁺, O₄⁺) become the dominant charged species. Generation and loss of ROS (O, O(¹D), O(¹S), O₂(a¹Δ_g), O₂(b¹Σ_g⁺), O₃) relevant for biomedical applications are discussed.



Introduction

Thanks to their low cost and easy implementation, atmospheric pressure plasmas have potential advantages over their low-pressure counterparts for a myriad of applications, such as plasma medicine,^[1,2] air purification,^[3,4] sterilization,^[5,6] surface modification,^[7,8] and water treatment.^[9,10] Various plasma chemistries have been investigated in recent years, and among them, He + O₂ has received large attention. He + O₂ plasmas combine the high thermal conductivity of He that helps keeping the gas temperature close to room temperature, with the oxidative power of oxygen-derived species (e.g. atomic oxygen and

ozone). Therefore, He + O₂ discharges provide a low-temperature reactive environment well suited for the oxidative treatment of temperature-sensitive surfaces, such as biological materials.^[1,11] Oxygen containing plasmas have been extensively studied for decades and they have enabled advances in material processing,^[12] environmental applications,^[13] and discharge lasers.^[14,15] Low-temperature atmospheric-pressure He + O₂ plasmas explored in the emerging field of plasma medicine, however, have attracted attention only in recent years, and their physics and chemistry remain to be fully unraveled. A better understanding of the physicochemical properties of these discharges would benefit further developments in this fast developing field.^[1,2]

In this contribution, we report on a global model of a low-temperature atmospheric-pressure diffuse He + O₂ glow discharge aimed at unraveling the chemistry at play in this kind of plasmas. The model extends the work of existing low-pressure global models,^[16,17] and incorporates reactions, such as three body collisions that become important at atmospheric pressure. The model also extends the chemistry model of an atmospheric pressure He + O₂ plasma proposed by Park et al.^[18,19] and within the simplicity of a zero dimensional model it also makes a more realistic approximation accounting for quasineutrality in the bulk

D.-X. Liu, M.-Z. Rong, X.-H. Wang
State Key Laboratory of Electrical Insulation and Power
Equipment, Xi'an Jiaotong University, 710049, P. R. China
F. Iza, M. G. Kong
Department of Electronic and Electrical Engineering,
Loughborough University, LE11 3TU, UK
Fax: +44 (0)1509 227014; E-mail: f.iza@lboro.ac.uk
P. Bruggeman
Department of Applied Physics, Eindhoven University of
Technology, PO Box 513, 5600 MB Eindhoven, The Netherlands

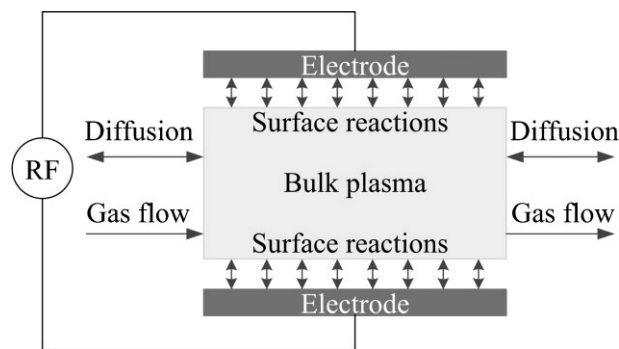
plasma, collisionality in the sheaths, energy flux to the electrodes, energy loss in elastic collisions (a dominant energy dissipation mechanism at atmospheric pressure) and relaxes the assumption of a Maxwellian electron energy distribution. The model includes 21 species and 267 reactions, and, based on the analysis of the simulation results, main species and reactions are selected to create simplified models that are able to capture the main physicochemical processes in the discharge, but with reduced numerical complexity. It is noted that, although the full model is able to address both active plasmas and afterglows, the simplified models given here are valid only for studying the active plasma region. Afterglows of atmospheric pressure discharges often take place in open air, and therefore the chemistry is not longer limited to that of the feed gas, and different physicochemical processes will take place. He + O₂ plasmas are found to undergo mode transitions as the oxygen concentration increases. As a result, 3 simplified models are created to model the discharge in different oxygen concentration regimes. While 13 species and 24 reactions are sufficient to capture the main chemistry of the discharge when the oxygen concentration is between 1 and 10 parts per million (ppm), 17 species and 41 reactions are needed when the oxygen concentration is between 10 and 5 000 ppm, and 15 species and 50 reactions when the oxygen concentration is between 0.5% and 10%. The accuracy of the simplified models is quantified by comparing simulation results of the simplified models against the model that incorporates the 267 reactions. The robustness of the simplified models to changes in the discharge geometry, gas temperature, and input power is also assessed, and it is found that the simplified models reduce the number of reactions by a factor of 5 – 11, while providing results that remain within a 20% of the results obtained with the detailed model. Therefore, the simplified models provide a valuable subset of reactions that can be incorporated in simulations, where computational cost prevents the use of complex chemistry models.

The manuscript is structured as follows. First, a description of the global model is given, followed by simulation results as a function of the oxygen concentration in the feed gas. Simplified models are introduced next and their accuracy assessed. And finally, the main physicochemical processes in He + O₂ atmospheric pressure discharges and the generation of reactive oxygen species are analyzed.

The Global Model

Global models have been widely used for analyzing the chemistry at play in low-temperature plasmas.^[12,18–20] In this kind of models, the spatial derivatives in the plasma are neglected (i.e. global models are volume-averaged models), and therefore the computational load is dramatically

reduced. This allows complex chemistry models with a large number of species and reactions to be studied. The schematic diagram of the He + O₂ discharge studied in this work is illustrated in Figure 1. It consists of two circular electrodes with radius $r = 1\text{ cm}$, separated by a gap $g = 0.1\text{ cm}$. The plasma is RF excited with an average power density of $40\text{ W} \cdot \text{cm}^{-3}$. The neutral gas temperature is set to remain at room temperature (300 K), and the gas flow rate is 100 sccm. Throughout the paper, these parameters are kept constant unless indicated otherwise. It is noted that these conditions are similar to the ones used in the experimental work of Liu et al.^[21] In order to investigate the effect of oxygen on the physicochemical properties of the He + O₂ discharge, a large range of oxygen concentrations ranging from 1 ppm to 10% (10^5 ppm) is analyzed in this work. For each species in the plasma, the plasma loses particles due to chemical reactions in the plasma volume, fluxes to the electrodes, sidewise diffusion and advection (Figure 1). As a result of the diffusion and advection transport, long lived neutral species, such as O₃, can be extracted from the plasma. The sidewise diffusion and advection of neutrals are usually neglected when modelling low pressure plasmas,^[17] but for atmospheric pressure plasmas where diffusion to the electrodes is slow and stable (long lived) species are generated, these loss mechanisms need to be considered. For charged species, however, since the thermal and gas flow velocities are small compared to the drift velocity, their sidewise flux is set to zero in the model. 21 species are incorporated in the model, and these are listed in Table 1. The list combines species considered in other studies of low-pressure and atmospheric-pressure plasmas with related chemistries: O₂,^[17,22] He,^[23,24] air,^[25] Ar + O₂,^[17,26] He + air,^[27] and He + O₂.^[18,21] The importance of each species is then studied as a function of the oxygen concentration in the discharge. The model incorporates 267 reactions, which are listed in Table 2. Most reaction rate coefficients are taken from the literature and all the electron-neutral two-body reaction rate coefficients are calculated based on cross section data. Where data is not available, the cross section is estimated by shifting cross sections by the required threshold



■ Figure 1. Schematic of the plasma set up use in this study.

Table 1. The 21 species included in the global model.

Species	Model ^{a)}	Species ^{b)}	Model
e	S	He	S
He ⁺	S1	O ₂	S
He ₂ ⁺	S1	He*	S1,S2
O ⁺		He ₂ *	S1,S2
O ⁻	S2,S3	O	S
O ₂ ⁺	S	O(¹ D)	S
O ₂ ⁻	S2,S3	O(¹ S)	S2,S3
O ₃ ⁻	S2,S3	O ₂ (b)	S
O ₄ ⁺	S2,S3	O ₂ (a)	S
O ₄ ⁻		O ₂ (ν)	S
		O ₃	S2,S3

^{a)}S1: main species in regime RG1; S2: main species in regime RG2; S3: main species in regime RG3; S: main species in RG1, RG2 and RG3; ^{b)}O₂(a) and O₂(b) represent O₂(a₁Δg) and O₂(b¹Σ_g⁺), respectively. O₂(ν) denotes the vibrational excited states of O₂ (ν = 1,2,3,4).

energy, as suggested in ref.^[18] Some of the ion-ion recombination rate coefficients are also estimated according to the recommendations made in refs.^[30,31] The Boltzmann solver BOLSIG+^[28] is used to determine the electron energy distribution function, and calculate the rate coefficients of electron impact reactions as a function of the electron mean energy and the feed gas composition. On the other hand, for heavy-particle reactions, the particle energy distribution is assumed to be Maxwellian. In the model, the time evolution of the density of each species in the plasma is governed by the particle balance equation.^[13,23,29]

$$\frac{dn_k}{dt} = G_k^V + \frac{S_1}{V} \left(\sum_{i=1, i \neq k}^N \alpha_{i,k} \Gamma_{1i} - \beta_k \Gamma_{1k} \right) - \frac{S_2}{V} \Gamma_{2k} - \frac{F}{V} n_k \quad (1)$$

where n_k (m⁻³) is the number density of species k , G_k^V (m⁻³ · s⁻¹) the net generation/loss rate of species k due to reactions in the bulk plasma, N the total number of species, S_1 (m²) the total area of the electrodes, S_2 (m²) the “sidewall” area, V (m³) the plasma volume, Γ_{1k} (m⁻² · s⁻¹) and Γ_{2k} (m⁻² · s⁻¹) the fluxes of species k to the electrodes and to the sides out of the plasma, and F (m³ · s⁻¹) the gas flow rate. For charged species, Γ_{2k} and F are assumed to be zero as for the conditions of interest here the drift velocity of the charged species is much larger than the thermal and advection velocities. The second term on the right-hand

side of Equation 1 represents the particle gain/loss due to surface reactions (see Table 3). β_k is the surface reaction probability of species k , and $\alpha_{i,k}$ a parameter between zero and one that relates to the generation probability of species k due to surface reactions of species i . For instance, O(¹D) + Wall → O has a probability of 1 (Table 3); therefore, $\alpha_{i,k}$ where k denotes O, and i denotes O(¹D) is equal to 1. It is noted that no secondary electron emissions have been considered in the model, although it is recognized that these can affect the discharge properties depending on the frequency of operation and the input power.^[30,31]

Regarding fluxes to the electrodes, the following assumptions are made: neutral species are assumed to be Maxwellian distributed, i.e. $\Gamma_n = 0.25 n_n v_{th}$; negative ions are assumed to be confined by the ambipolar field, i.e. $\Gamma_- = 0$; and the flux of positive ions is assumed to be given by $\Gamma_+ = 0.6 n_+ u_s$, where u_s is the velocity of the ions at the entrance of a collisional sheath.^[13] For typical atmospheric pressure plasmas, the ion velocity at the sheath edge (u_s) can be more than an order of magnitude smaller than the Bohm velocity, and therefore the use of the collisionless sheath formula (Bohm velocity) would result in an overestimation of the particle losses, leading to an increase in the mean electron energy. The prefactor 0.6 in the above flux formula accounts for the drop in plasma density that occurs from the centre of the discharge to the sheath edge. A voltage drop across the presheath of $1/2T_e$ is assumed in obtaining the prefactor 0.6. The actual voltage drop, however, ultimately depends on the presheath geometry, its collisionality and the plasma heating mechanisms.^[32] Finally, the electron flux is set to balance the positive ion flux, maintaining quasineutrality in the bulk plasma, i.e. $\Gamma_e = \sum \Gamma_+$. To solve the particle balance equation, the mean electron energy is needed, as this is required to compute the various generation/loss rates. In the model, the electron energy is obtained by solving the following power balance equation.^[13,23,29]

$$\frac{d}{dt} \left(\frac{3}{2} n_e T_e \right) = \frac{P_{in}}{eV} - \sum_{i=1}^{N_r} \varepsilon_i R_i - \frac{S_1}{V} \left(\varepsilon_e \Gamma_e + \sum_{j=1}^{N_p} \varepsilon_p \Gamma_{1j} \right) \quad (2)$$

where e is the elementary charge, P_{in} (W) is the time-average input power, N_r the number of electron impact reactions, ε_i (eV) and R_i (m⁻³ · s⁻¹) the electron energy loss due to the i th electron impact reaction and the corresponding reaction rate, ε_e (eV) the electron energy loss per electron escaping the plasma and ε_p (eV) the energy loss per ion that crosses the sheath. In this model, ε_e is assumed to be $2T_e$,^[13] and ε_p 100 eV. It is worth noting that, although ions reach the electrodes with little kinetic energy due to collisions in the sheath (typically < 1eV),^[33,34] the energy

Table 2. Chemical reactions included in the models.

No	Reaction ^{a)}	Rate coefficient ^{b)}	Note ^{c)}	Ref
1	$e + He \rightarrow e + He$	$f(T_e)$	S	[59]
2	$e + O_2 \rightarrow e + O_2$	$f(T_e)$	S3	[60]
3	$e + He \rightarrow He^+ + 2e$	$f(T_e)$	S1	[59]
4	$e + He^* \rightarrow He^+ + 2e$	$f(T_e)$	S1	[61]
5	$e + He_2^* \rightarrow He_2^+ + 2e$	$9.75 \times 10^{-10} T_e^{0.71} \exp(-3.4/T_e)$		[62]
6	$e + O \rightarrow O^+ + 2e$	$f(T_e)$		[63]
7	$e + O(^1D) \rightarrow O^+ + 2e$	$f(T_e)$		d)
8	$e + O(^1S) \rightarrow O^+ + 2e$	$f(T_e)$		d)
9	$e + O^- \rightarrow O + 2e$	$f(T_e)$		[64]
10	$e + O_2 \rightarrow O_2^+ + 2e$	$f(T_e)$	S	[54]
11	$e + O_2 \rightarrow O^+ + O + 2e$	$f(T_e)$		[54]
12	$e + O_2(a) \rightarrow O_2^+ + 2e$	$f(T_e)$		d)
13	$e + O_2(a) \rightarrow O^+ + O + 2e$	$f(T_e)$		d)
14	$e + O_2(b) \rightarrow O_2^+ + 2e$	$f(T_e)$		d)
15	$e + O_2(b) \rightarrow O + O^+ + 2e$	$f(T_e)$		d)
16	$e + O_2(v) \rightarrow O_2^+ + 2e$	$f(T_e)$		d)
17	$e + O_2(v) \rightarrow O^+ + O + 2e$	$f(T_e)$		d)
18	$e + He \rightarrow e + He^*$	$f(T_e)$	S1,S2	[59]
19	$e + He^* \rightarrow e + He$	$f(T_e)$		e)
20	$e + He_2^* \rightarrow e + 2He$	3.8×10^{-9}		[25]
21	$e + O \rightarrow O(^1D) + e$	$f(T_e)$		[63]
22	$e + O(^1D) \rightarrow O + e$	$f(T_e)$		e)
23	$e + O \rightarrow O(^1S) + e$	$f(T_e)$	S2,S3	[63]
24	$e + O(^1S) \rightarrow O + e$	$f(T_e)$		e)
25	$e + O_2 \rightarrow 2O + e$	$f(T_e)$	S	[15]
26	$e + O_2 \rightarrow O(^1D) + O + e$	$f(T_e)$	S	[54]
27	$e + O_2 \rightarrow O(^1S) + O + e$	$f(T_e)$	S2,S3	[65]
28	$e + O_2 \rightarrow O_2(b) + e$	$f(T_e)$	S	[60]
29	$e + O_2 \rightarrow O_2(a) + e$	$f(T_e)$	S	[60]
30	$e + O_2 \rightarrow O_2(v) + e$	$f(T_e)$	S	[59]
31	$e + O_2(a) \rightarrow O_2(b) + e$	$f(T_e)$		[66]
32	$e + O_2(a) \rightarrow O(^1D) + O + e$	$f(T_e)$		[15]
33	$e + O_2(a) \rightarrow O(^1S) + O + e$	$f(T_e)$		d)
34	$e + O_2(a) \rightarrow 2O + e$	$f(T_e)$		d)
35	$e + O_2(a) \rightarrow O_2 + e$	$f(T_e)$		e)
36	$e + O_2(b) \rightarrow O(^1D) + O + e$	$f(T_e)$		d)
37	$e + O_2(b) \rightarrow O(^1S) + O + e$	$f(T_e)$		d)
38	$e + O_2(b) \rightarrow 2O + e$	$f(T_e)$		d)
39	$e + O_2(b) \rightarrow O_2 + e$	$f(T_e)$		e)
40	$e + O_2(v) \rightarrow O_2(a^1\Delta_g) + e$	$f(T_e)$		d)
41	$e + O_2(v) \rightarrow O_2(b^1\Sigma_g^+) + e$	$f(T_e)$		d)

Table 2. (Continued)

No	Reaction ^{a)}	Rate coefficient ^{b)}	Note ^{c)}	Ref
42	$e + O_2(v) \rightarrow 2O + e$	$f(T_e)$		d)
43	$e + O_2(v) \rightarrow O(^1D) + O + e$	$f(T_e)$		d)
44	$e + O_2(v) \rightarrow O(^1S) + O + e$	$f(T_e)$		d)
45	$e + O_2(v) \rightarrow O_2 + e$	$f(T_e)$		e)
46	$e + O \rightarrow O^-$	$f(T_e)$		[67]
47	$e + O_2 \rightarrow O + O^-$	$f(T_e)$	S2,S3	[65]
48	$e + O_2(a) \rightarrow O + O^-$	$f(T_e)$		[68]
49	$e + O_2(b) \rightarrow O + O^-$	$f(T_e)$	S2,S3	[69]
50	$e + O_2(v) \rightarrow O^- + O$	$f(T_e)$		d)
51	$e + O_3 \rightarrow O + O_2^-$	$f(T_e)$		[65]
52	$e + O_3 \rightarrow O^- + O_2$	$f(T_e)$	S3	[65]
53	$e + He^+ \rightarrow He^*$	$6.76 \times 10^{-13} T_e^{-0.5}$		[18]
54	$e + He_2^+ \rightarrow He^* + He$	$7.12 \times 10^{-15} (T_e/T_g)^{-1.5}$		[70]
55	$e + O^+ \rightarrow O(^1D)$	$5.3 \times 10^{-13} T_e^{-0.5}$		[18]
56	$e + O_2^+ \rightarrow O + O$	$1.2 \times 10^{-8} T_e^{-0.7}$		[18]
57	$e + O_2^+ \rightarrow O + O(^1D)$	$8.88 \times 10^{-9} T_e^{-0.7}$		[18]
58	$e + O_2^+ \rightarrow 2O(^1D)$	$6.87 \times 10^{-9} T_e^{-0.7}$		[27]
59	$e + O_4^+ \rightarrow 2O_2$	$2.25 \times 10^{-7} T_e^{-0.5}$	S2	[31]
60	$2e + He^+ \rightarrow He^* + e$	$7.8 \times 10^{-38} (T_e/T_g)^{-4.4}$		[40]
61	$2e + He_2^+ \rightarrow He^* + He + e$	2.8×10^{-20}		[25]
62	$2e + He_2^+ \rightarrow He_2^* + e$	1.2×10^{-21}		[25]
63	$2e + O^+ \rightarrow O + e$	$5.12 \times 10^{-27} T_e^{-4.5}$		[18]
64	$2e + O_2^+ \rightarrow O_2 + e$	$7.18 \times 10^{-27} T_e^{-4.5}$		[31]
65	$2e + O_4^+ \rightarrow 2O_2 + e$	$7.18 \times 10^{-27} T_e^{-4.5}$		[31]
66	$e + He^+ + He \rightarrow He^* + He$	$7.4 \times 10^{-35} (T_e/T_g)^{-2}$		[40]
67	$e + He_2^+ + He \rightarrow He^* + 2He$	3.5×10^{-27}	S1	[25]
68	$e + He_2^+ + He \rightarrow He_2^* + He$	1.5×10^{-27}		[25]
69	$e + O^+ + O_2 \rightarrow O + O_2$	$2.49 \times 10^{-29} T_e^{-1.5}$		[27]
70	$e + O^+ + He \rightarrow O + He$	$6.45 \times 10^{-31} T_e^{-2.5}$		[29]
71	$e + O_2^+ + O_2 \rightarrow 2O_2$	$2.49 \times 10^{-29} T_e^{-1.5}$		[27]
72	$e + O + O_2 \rightarrow O^- + O_2$	1.0×10^{-31}		[27]
73	$e + O + He \rightarrow O^- + He$	1.0×10^{-31}		f)
74	$e + O_2 + O_2 \rightarrow O_2^- + O_2$	$2.26 \times 10^{-30} (T_g/300)^{-0.5}$	S3	[20]
75	$e + O_2 + He \rightarrow O_2^- + He$	1×10^{-31}	S2,S3	[29]
76	$e + O_3 + O_2 \rightarrow O_3^- + O_2$	1.0×10^{-31}		[27]
77	$e + O_3 + He \rightarrow O_3^- + He$	1.0×10^{-31}		f)
78	$He^+ + O^- \rightarrow O + He$	$2 \times 10^{-7} (T_g/300)^{-1}$		[18]
79	$He^+ + O^- + M \rightarrow O + He + M$	$2 \times 10^{-25} (T_g/300)^{-2.5}$		[18]
80	$He^+ + O_2^- \rightarrow O_2 + He$	$2 \times 10^{-7} (T_g/300)^{-1}$		[18]

Table 2. (Continued)

No	Reaction ^{a)}	Rate coefficient ^{b)}	Note ^{c)}	Ref
81	$He^+ + O_3^- \rightarrow O_3 + He$	$2 \times 10^{-7} (T_g/300)^{-1}$		[18]
82	$He^+ + O_4^- + M \rightarrow He + 2O_2 + M$	$2 \times 10^{-25} (T_g/300)^{-2.5}$		[31]
83	$He_2^+ + O^- \rightarrow O + 2He$	1×10^{-7}		[31]
84	$He_2^+ + O^- + M \rightarrow O + 2He + M$	$2 \times 10^{-25} (T_g/300)^{-2.5}$		[31]
85	$He_2^+ + O_2^- \rightarrow O_2 + 2He$	1×10^{-7}		[31]
86	$He_2^+ + O_2^- + M \rightarrow O_2 + 2He + M$	$2 \times 10^{-25} (T_g/300)^{-2.5}$		[31]
87	$He_2^+ + O_3^- \rightarrow O_3 + 2He$	1×10^{-7}		[31]
88	$He_2^+ + O_3^- + M \rightarrow O_3 + 2He + M$	$2 \times 10^{-25} (T_g/300)^{-2.5}$		[31]
89	$He_2^+ + O_4^- + M \rightarrow 2He + 2O_2 + M$	$2 \times 10^{-25} (T_g/300)^{-2.5}$		[31]
90	$O^+ + O^- \rightarrow 2O$	$2 \times 10^{-7} (T_g/300)^{-1}$		[18]
91	$O^+ + O^- \rightarrow O + O(^1D)$	$4.9 \times 10^{-10} (T_g/300)^{-0.5}$		[45]
92	$O^+ + O^- + M \rightarrow 2O + M$	$2 \times 10^{-25} (T_g/300)^{-2.5}$		[18]
93	$O^+ + O_2^- \rightarrow O_2 + O$	$2.7 \times 10^{-7} (T_g/300)^{-0.5}$		[28]
94	$O^+ + O_2^- + M \rightarrow O_2 + O + M$	$2 \times 10^{-25} (T_g/300)^{-2.5}$		[31]
95	$O^+ + O_3^- \rightarrow O_3 + O$	$2 \times 10^{-7} (T_g/300)^{-1}$		[18]
96	$O^+ + O_3^- + M \rightarrow O_3 + O + M$	$2 \times 10^{-25} (T_g/300)^{-2.5}$		[31]
97	$O^+ + O_4^- + M \rightarrow O + 2O_2 + M$	$2 \times 10^{-25} (T_g/300)^{-2.5}$		[31]
98	$O_2^+ + O^- \rightarrow O_2 + O$	$2 \times 10^{-7} (T_g/300)^{-0.5}$		[27]
99	$O_2^+ + O^- + M \rightarrow O_2 + O + M$	$2 \times 10^{-25} (T_g/300)^{-2.5}$	S2,S3	[18]
100	$O_2^+ + O_2^- \rightarrow 2O_2$	$2.0 \times 10^{-7} (T_g/300)^{-0.5}$		[28]
101	$O_2^+ + O_2^- \rightarrow O_2 + 2O$	$1.01 \times 10^{-7} (T_g/300)^{-0.5}$		[28]
102	$O_2^+ + O_2^- + M \rightarrow 2O_2 + M$	$2 \times 10^{-25} (T_g/300)^{-2.5}$	S2,S3	[31]
103	$O_2^+ + O_3^- \rightarrow O_3 + 2O$	1×10^{-7}		[18]
104	$O_2^+ + O_3^- \rightarrow O_3 + O_2$	$2 \times 10^{-7} (T_g/300)^{-1}$		[18]
105	$O_2^+ + O_3^- + M \rightarrow O_3 + O_2 + M$	$2 \times 10^{-25} (T_g/300)^{-2.5}$	S2,S3	[31]
106	$O_2^+ + O_4^- + M \rightarrow 3O_2 + M$	$2 \times 10^{-25} (T_g/300)^{-2.5}$		[31]
107	$O_4^+ + O^- \rightarrow 2O_2 + O$	1×10^{-7}		[31]
108	$O_4^+ + O_2^- \rightarrow 3O_2$	1×10^{-7}		[31]
109	$O_4^+ + O_3^- \rightarrow 3O_2 + O$	1×10^{-7}		[31]
110	$O_4^+ + O^- + M \rightarrow 2O_2 + O + M$	$2 \times 10^{-25} (T_g/300)^{-2.5}$	S2,S3	[31]
111	$O_4^+ + O_2^- + M \rightarrow 3O_2 + M$	$2 \times 10^{-25} (T_g/300)^{-2.5}$	S2,S3	[31]
112	$O_4^+ + O_3^- + M \rightarrow 2O_2 + O_3 + M$	$2 \times 10^{-25} (T_g/300)^{-2.5}$	S2,S3	[31]
113	$O_4^+ + O_4^- + M \rightarrow 4O_2 + M$	$2 \times 10^{-25} (T_g/300)^{-2.5}$		[31]
114	$O^- + He \rightarrow He + O + e$	$2.5 \times 10^{-18} (T_g/300)^{0.6}$		[71]
115	$O^- + He^* \rightarrow O + He + e$	3×10^{-10}		[72]

Table 2. (Continued)

No	Reaction ^{a)}	Rate coefficient ^{b)}	Note ^{c)}	Ref
116	$O^- + He_2^* \rightarrow O + 2He + e$	3×10^{-10}		[72], ^{h)}
117	$O^- + O \rightarrow O_2 + e$	$2.0 \times 10^{-10} (T_g/300)^{0.5}$	S2,S3	[18]
118	$O^- + O(^1D) \rightarrow 2O + e$	1×10^{-10}		[72]
119	$O^- + O(^1S) \rightarrow 2O + e$	1×10^{-10}		[72]
120	$O^- + O_2(b) \rightarrow O_2 + O + e$	$6.9 \times 10^{-10} (T_g/300)^{0.5}$	S2,S3	[18]
121	$O^- + O_2(a) \rightarrow O_3 + e$	$3 \times 10^{-10} (T_g/300)^{0.5}$	S2,S3	[18]
122	$O^- + O_2 \rightarrow O_3 + e$	$5 \times 10^{-15} (T_g/300)^{0.5}$		[18]
123	$O^- + O_3 \rightarrow 2O_2 + e$	$3.01 \times 10^{-10} (T_g/300)^{0.5}$		[18]
124	$O_2^- + He \rightarrow He + O_2 + e$	$3.9 \times 10^{-10} \exp(-7400/T_g)$		[73]
125	$O_2^- + He^* \rightarrow O_2 + He + e$	3×10^{-10}		[72]
126	$O_2^- + He_2^* \rightarrow O_2 + 2He + e$	3×10^{-10}		[72], ^{h)}
127	$O_2^- + O \rightarrow O_3 + e$	$1.5 \times 10^{-10} (T_g/300)^{0.5}$	S3	[18]
128	$O_2^- + O(^1D) \rightarrow O + O_2 + e$	1×10^{-10}		[72]
129	$O_2^- + O(^1S) \rightarrow O + O_2 + e$	1×10^{-10}		[72]
130	$O_2^- + O_2 \rightarrow 2O_2 + e$	$2.7 \times 10^{-10} \exp(-5590/T_g)$		[74]
131	$O_2^- + O_2(b) \rightarrow 2O_2 + e$	3.6×10^{-10}	S3	[27]
132	$O_2^- + O_2(a) \rightarrow 2O_2 + e$	$2.0 \times 10^{-10} (T_g/300)^{0.5}$		[18]
133	$O_3^- + He^* \rightarrow O + O_2 + He + e$	3×10^{-10}		[72]
134	$O_3^- + He_2^* \rightarrow O + O_2 + 2He + e$	3×10^{-10}		[72]
135	$O_3^- + O \rightarrow 2O_2 + e$	1×10^{-11}		[72]
136	$O_3^- + O(^1S) \rightarrow O + O_3 + e$	1×10^{-10}		[72]
137	$O_4^- + He^* \rightarrow 2O_2 + He + e$	1×10^{-10}		[72]
138	$O_4^- + He_2^* \rightarrow 2O_2 + 2He + e$	1×10^{-10}		[72]
139	$O_4^- + O(^1D) \rightarrow O + 2O_2 + e$	1×10^{-10}		[72]
140	$O_4^- + O(^1S) \rightarrow O + 2O_2 + e$	1×10^{-10}		[72]
141	$O_4^- + O_2(b^1\Sigma_g^+) \rightarrow 3O_2 + e$	1×10^{-10}		[72]
142	$He^+ + 2He \rightarrow He_2^+ + He$	$1.4 \times 10^{-31} (T_g/300)^{-0.6}$	S1	[40]
143	$He^+ + O \rightarrow O^+ + He$	$5 \times 10^{-11} (T_g/300)^{0.5}$		[18]
144	$He^+ + O(^1D) \rightarrow O^+ + He$	$5 \times 10^{-11} (T_g/300)^{0.5}$		[18]
145	$He^+ + O(^1S) \rightarrow O^+ + He$	$5 \times 10^{-11} (T_g/300)^{0.5}$		[18]
146	$He^+ + O_2 \rightarrow O^+ + O + He$	$1.07 \times 10^{-9} (T_g/300)^{0.5}$		[18]
147	$He^+ + O_2 \rightarrow O_2^+ + He$	$3.3 \times 10^{-11} (T_g/300)^{0.5}$		[18]
148	$He^+ + O_2(a) \rightarrow O^+ + O + He$	$1.07 \times 10^{-9} (T_g/300)^{0.5}$		[18]
149	$He^+ + O_2(a) \rightarrow O_2^+ + He$	$3.3 \times 10^{-11} (T_g/300)^{0.5}$		[18]
150	$He^+ + O_3 \rightarrow O^+ + O_2 + He$	$1.07 \times 10^{-9} (T_g/300)^{0.5}$		[18]
151	$He_2^+ + O \rightarrow O^+ + 2He$	$1 \times 10^{-9} (T_g/300)^{0.5}$		f)

Table 2. (Continued)

No	Reaction ^{a)}	Rate coefficient ^{b)}	Note ^{c)}	Ref
152	$He_2^+ + O(^1D) \rightarrow O^+ + 2He$	$1 \times 10^{-9} (T_g/300)^{0.5}$		f)
153	$He_2^+ + O(^1S) \rightarrow O^+ + 2He$	$1 \times 10^{-9} (T_g/300)^{0.5}$		f)
154	$He_2^+ + O_2 \rightarrow O_2^+ + 2He$	$1 \times 10^{-9} (T_g/300)^{0.5}$	S1	[75]
155	$He_2^+ + O_2(b) \rightarrow O_2^+ + 2He$	$1 \times 10^{-9} (T_g/300)^{0.5}$		f)
156	$He_2^+ + O_2(a) \rightarrow O_2^+ + 2He$	$1 \times 10^{-9} (T_g/300)^{0.5}$		f)
157	$He_2^+ + O_3 \rightarrow O^+ + O_2 + 2He$	$1 \times 10^{-9} (T_g/300)^{0.5}$		f)
158	$O^+ + O + M \rightarrow O_2^+ + M$	$1 \times 10^{-29} (T_g/300)^{0.5}$		[18]
159	$O^+ + O_2 \rightarrow O_2^+ + O$	$2.0 \times 10^{-11} (T_g/300)^{-0.5}$		[45]
160	$O^+ + O_3 \rightarrow O_2^+ + O_2$	1×10^{-10}		[18]
161	$O^- + O_2(a) \rightarrow O_2^- + O$	$1.1 \times 10^{-11} (T_g/300)^{-0.5}$		[45]
162	$O^- + O_3 \rightarrow O_2^- + O_2$	$1.02 \times 10^{-11} (T_g/300)^{0.5}$		[18]
163	$O^- + O_3 \rightarrow O_3^- + O$	$1.99 \times 10^{-10} (T_g/300)^{0.5}$		[18]
164	$O^- + O_2 + M \rightarrow O_3^- + M$	$1.1 \times 10^{-30} (T_g/300)^{-1}$		[72]
165	$O_2^+ + He^* \rightarrow O^+ + O + He$	1×10^{-10}		[72]
166	$O_2^+ + He_2^* \rightarrow O^+ + O + 2He$	1×10^{-10}		[72]
167	$O_2^+ + O(^1D) \rightarrow O_2(a) + O^+$	$1 \times 10^{-12} (T_g/300)^{-0.5}$		[45]
168	$O_2^+ + 2O_2 \rightarrow O_4^+ + O_2$	$2.4 \times 10^{-30} (T_g/300)^{-3.2}$	S3	[31]
169	$O_2^+ + O_2 + He \rightarrow O_4^+ + He$	$5.8 \times 10^{-31} (T_g/300)^{-3.1}$	S2,S3	[76]
170	$O_2^- + O \rightarrow O^- + O_2$	$1.5 \times 10^{-10} (T_g/300)^{0.5}$		[18]
171	$O_2^- + O_3 \rightarrow O_3^- + O_2$	$6 \times 10^{-10} (T_g/300)^{0.5}$	S3	[18]
172	$O_2^- + O(^1S) \rightarrow O^- + 2O$	1×10^{-10}		[72]
173	$O_2^- + O_2 + M \rightarrow O_4^- + M$	$3.5 \times 10^{-31} (T_g/300)^{-1}$		[31]
174	$O_3^- + O \rightarrow O_2^- + O_2$	$2.5 \times 10^{-10} (T_g/300)^{0.5}$	S2,S3	[18]
175	$O_3^- + O(^1D) \rightarrow O^- + O + O_2$	1×10^{-10}		[72]
176	$O_3^- + O(^1S) \rightarrow O^- + O + O_2$	1×10^{-10}		[72]
177	$O_3^- + O(^1S) \rightarrow O_2^- + 2O$	1×10^{-10}		[72]
178	$O_3^- + O_2(b^1\Sigma_g^+) \rightarrow O^- + 2O_2$	1×10^{-10}		[72]
179	$O_4^+ + He^* \rightarrow O^+ + O + O_2 + He$	1×10^{-10}		[72]
180	$O_4^+ + He_2^* \rightarrow O^+ + O + O_2 + 2He$	1×10^{-10}		[72]
181	$O_4^+ + O \rightarrow O_2^+ + O_3$	3×10^{-10}	S2,S3	[31]
182	$O_4^+ + O(^1D) \rightarrow O_2^+ + O_3$	3×10^{-10}		g)
183	$O_4^+ + O(^1S) \rightarrow O_2^+ + O_3$	3×10^{-10}		g)
184	$O_4^+ + O_2 \rightarrow O_2^+ + 2O_2$	$3.3 \times 10^{-6} \left(\frac{T_g}{300}\right)^{-4} \exp\left(-\frac{5030}{T_g}\right)$	S2,S3	[31]
185	$O_4^+ + O_2(a) \rightarrow O_2^+ + 2O_2$	1×10^{-10}		[31]
186	$O_4^+ + O_2(b) \rightarrow O_2^+ + 2O_2$	1×10^{-10}		[31]

Table 2. (Continued)

No	Reaction ^{a)}	Rate coefficient ^{b)}	Note ^{c)}	Ref
187	$O_4^+ + He \rightarrow O_2^+ + O_2 + He$	3×10^{-17}		[77]
188	$O_4^- + M \rightarrow O_2^- + O_2 + M$	$1 \times 10^{-10} \exp(-1044/T_g)$		[31]
189	$O_4^- + O \rightarrow O_3^- + O_2$	4×10^{-10}		[31]
190	$O_4^- + O \rightarrow O^- + 2O_2$	3×10^{-10}		[31]
191	$O_4^- + O(^1D) \rightarrow O_2^- + O_2 + O$	1×10^{-10}		[72]
192	$O_4^- + O(^1S) \rightarrow O^- + 2O_2$	1×10^{-10}		[72]
193	$O_4^- + O_2(a^1\Delta_g) \rightarrow O_2^- + 2O_2$	1×10^{-10}		[31]
194	$O_4^- + O_2(b^1\Sigma_g^+) \rightarrow O_2^- + 2O_2$	1×10^{-10}		[31]
195	$O_4^- + O_3 \rightarrow O_3^- + 2O_2$	3×10^{-10}		[31]
196	$2He^* \rightarrow He_2^+ + e$	$2.03 \times 10^{-9} (T_g/300)^{0.5}$	S1	[40]
197	$2He^* \rightarrow He^+ + He + e$	$8.7 \times 10^{-10} (T_g/300)^{0.5}$	S1	[40]
198	$He^* + He_2^* \rightarrow He^+ + 2He + e$	$5 \times 10^{-10} (T_g/300)^{0.5}$		[25]
199	$He^* + He_2^* \rightarrow He_2^+ + He + e$	$2 \times 10^{-9} (T_g/300)^{0.5}$	S1	[25]
200	$2He_2^* \rightarrow He^+ + 3He + e$	$3 \times 10^{-10} (T_g/300)^{0.5}$	S1	[25]
201	$2He_2^* \rightarrow He_2^+ + 2He + e$	$1.2 \times 10^{-9} (T_g/300)^{0.5}$	S1	[25]
202	$He^* + O \rightarrow O^+ + He + e$	$3.96 \times 10^{-10} (T_g/300)^{0.17}$		[75]
203	$He^* + O(^1D) \rightarrow O^+ + He + e$	$3.96 \times 10^{-10} (T_g/300)^{0.17}$		[75]
204	$He^* + O(^1S) \rightarrow O^+ + He + e$	$3.96 \times 10^{-10} (T_g/300)^{0.17}$		[75]
205	$He^* + O_2 \rightarrow O_2^+ + He + e$	$2.54 \times 10^{-10} (T_g/300)^{0.5}$	S1,S2	[18]
206	$He^* + O_2(b) \rightarrow O_2^+ + He + e$	$2.54 \times 10^{-10} (T_g/300)^{0.5}$		[18]
207	$He^* + O_3 \rightarrow O_2^+ + O + He + e$	$2.54 \times 10^{-10} (T_g/300)^{0.5}$		[18]
208	$He_2^* + O \rightarrow O^+ + 2He + e$	$1 \times 10^{-10} (T_g/300)^{0.5}$		†)
209	$He_2^* + O(^1D) \rightarrow O^+ + 2He + e$	$1 \times 10^{-10} (T_g/300)^{0.5}$		†)
210	$He_2^* + O(^1S) \rightarrow O^+ + 2He + e$	$1 \times 10^{-10} (T_g/300)^{0.5}$		†)
211	$He_2^* + O_2 \rightarrow O_2^+ + 2He + e$	$1 \times 10^{-10} (T_g/300)^{0.5}$	S1,S2	[75]
212	$He_2^* + O_3 \rightarrow O_2^+ + O + 2He + e$	$1 \times 10^{-10} (T_g/300)^{0.5}$		†)
213	$He_2^* + M \rightarrow 2He + M$	1.5×10^{-15}	S1,S2	[70]
214	$O(^1D) + O \rightarrow 2O$	8×10^{-12}		[18]
215	$O(^1D) + O_2 \rightarrow O + O_2$	$4.8 \times 10^{-12} \exp(67/T_g)$	S2,S3	[78]
216	$O(^1D) + O_2 \rightarrow O + O_2(a)$	$1.6 \times 10^{-12} \exp(67/T_g)$	S2,S3	[78]
217	$O(^1D) + O_2 \rightarrow O + O_2(b)$	$2.56 \times 10^{-11} \exp(67/T_g)$	S2,S3	[78]
218	$O(^1D) + O_3 \rightarrow 2O_2$	1.2×10^{-10}		[18]
219	$O(^1D) + O_3 \rightarrow 2O + O_2$	1.2×10^{-10}		[18]
220	$O(^1D) + He \rightarrow O + He$	1.0×10^{-13}	S	[18]
221	$O(^1S) + O \rightarrow O(^1D) + O$	$1.67 \times 10^{-11} \exp(-300/T_g)$		[18]
222	$O(^1S) + O \rightarrow 2O$	$3.33 \times 10^{-11} \exp(-300/T_g)$		[18]

Table 2. (Continued)

No	Reaction ^{a)}	Rate coefficient ^{b)}	Note ^{c)}	Ref
223	$O(^1S) + O_2 \rightarrow O + O_2$	$1.6 \times 10^{-12} \exp(-850/T_g)$	S3	[18]
224	$O(^1S) + O_2 \rightarrow O(^1D) + O_2$	$3.2 \times 10^{-12} \exp(-850/T_g)$	S3	[18]
225	$O(^1S) + O_2(a) \rightarrow O + O_2$	1.1×10^{-10}	S2,S3	[18]
226	$O(^1S) + O_2(a) \rightarrow 3O$	3.2×10^{-11}		[18]
227	$O(^1S) + O_2(a) \rightarrow O(^1D) + O_2(b)$	2.9×10^{-11}		[18]
228	$O(^1S) + O_3 \rightarrow 2O_2$	4.63×10^{-10}	S3	[79]
229	$O_2(a) + O \rightarrow O_2 + O$	7.0×10^{-16}		[27]
230	$O_2(a) + O_2 \rightarrow 2O_2$	$2.2 \times 10^{-18} (T_g/300)^{0.8}$		[27]
231	$O_2(a) + O_2 \rightarrow O + O_3$	$2.95 \times 10^{-21} (T_g/300)^{0.5}$		[18]
232	$2O_2(a) \rightarrow 2O_2$	$9 \times 10^{-17} \exp(-560/T_g)$		[18]
233	$2O_2(a) \rightarrow O_2(b) + O_2$	$9 \times 10^{-17} \exp(-560/T_g)$		[18]
234	$O_2(a) + O_3 \rightarrow 2O_2 + O$	$5.2 \times 10^{-11} \exp(-2840/T_g)$		[79]
235	$O_2(a) + He \rightarrow O_2 + He$	$8 \times 10^{-21} (T_g/300)^{0.5}$		[18]
236	$O_2(b) + O \rightarrow O_2 + O$	$8.0 \times 10^{-15} (T_g/300)^{0.5}$		[18]
237	$O_2(b) + O \rightarrow O_2(a) + O$	$7.2 \times 10^{-14} (T_g/300)^{0.5}$		[18]
238	$O_2(b) + O_2 \rightarrow 2O_2$	$4.0 \times 10^{-18} (T_g/300)^{0.5}$		[18]
239	$O_2(b) + O_2 \rightarrow O_2(a) + O_2$	$3.6 \times 10^{-17} (T_g/300)^{0.5}$		[18]
240	$2O_2(b) \rightarrow O_2(a) + O_2$	$3.6 \times 10^{-17} (T_g/300)^{0.5}$		[18]
241	$O_2(b) + O_3 \rightarrow 2O_2 + O$	$7.33 \times 10^{-12} (T_g/300)^{0.5}$	S2,S3	[18]
242	$O_2(b) + O_3 \rightarrow O_2(a) + O_3$	$7.33 \times 10^{-12} (T_g/300)^{0.5}$	S3	[18]
243	$O_2(b) + O_3 \rightarrow O_2 + O_3$	$7.33 \times 10^{-12} (T_g/300)^{0.5}$	S3	[18]
244	$O_2(b) + He \rightarrow O_2(a) + He$	$1 \times 10^{-17} (T_g/300)^{0.5}$		[18]
245	$O_2(v) + O \rightarrow O_2 + O$	$1 \times 10^{-14} (T_g/300)^{0.5}$		[8]
246	$O_2(v) + M \rightarrow O_2 + M$	$1 \times 10^{-14} (T_g/300)^{0.5}$	S	[18]
247	$O_3 + O \rightarrow 2O_2$	$8 \times 10^{-12} \exp(-2060/T_g)$		[79]
248	$O_3 + M \rightarrow O_2 + O + M$	$1.56 \times 10^{-9} \exp(-11490/T_g)$		[18]
249	$He^* + 2He \rightarrow He_2^* + He$	2×10^{-34}	S1,S2	[70]
250	$3O \rightarrow O + O_2$	$9.21 \times 10^{-34} (T_g/300)^{-0.63}$		[18]
251	$3O \rightarrow O + O_2(a)$	$6.93 \times 10^{-35} (T_g/300)^{-0.63}$		[18]
252	$2O + O_2 \rightarrow 2O_2$	$2.56 \times 10^{-34} (T_g/300)^{-0.63}$		[18]
253	$2O + O_2 \rightarrow O_2 + O_2(a)$	$1.93 \times 10^{-35} (T_g/300)^{-0.63}$		[18]
254	$2O + O_2 \rightarrow O_3 + O$	$3.4 \times 10^{-34} \exp(345/T_g)$		[80]
255	$2O + O_2(a) \rightarrow O_2 + O_2(a)$	7.4×10^{-33}		[80]
256	$2O + He \rightarrow He + O_2$	$1.3 \times 10^{-32} \left(\frac{T_g}{300}\right)^{-1} \exp\left(-\frac{170}{T_g}\right)$		[29]
257	$2O + He \rightarrow O_2(a) + He$	9.88×10^{-35}		[18]

Table 2. (Continued)

No	Reaction ^{a)}	Rate coefficient ^{b)}	Note ^{c)}	Ref
258	$O + 2O_2 \rightarrow O_3 + O_2$	$6 \times 10^{-34} (T_g/300)^{-2.8}$	S3	[18]
259	$O + O_2 + He \rightarrow O_3 + He$	$1.1 \times 10^{-34} \exp(510/T_g)$	S2,S3	[29]
260	$O + O_3 + O_2 \rightarrow 2O_3$	$1.5 \times 10^{-34} \exp(710/T_g)$		[27]
261	$O + O_2(a) + O_2 \rightarrow 2O_2 + O$	1×10^{-32}		[28]
262	$O + O_2(a) + He \rightarrow O_2 + O + He$	1×10^{-32}	S3	[28], ^{f)}
263	$2O_2(a) + O_2 \rightarrow 2O_3$	1×10^{-31}		[80]
264	$O(^1D) \rightarrow O + h\nu$	$5.0 \times 10^{-3} s^{-1}$		[27]
265	$O(^1S) \rightarrow O(^1D) + h\nu$	$1.34 s^{-1}$		[27]
266	$O_2(a) \rightarrow O_2 + h\nu$	$2.7 \times 10^{-4} s^{-1}$		[81]
267	$O_2(b) \rightarrow O_2 + h\nu$	$8.3 \times 10^{-2} s^{-1}$		[82]

^{a)}He* represents He(2³S) and He(2¹S); He₂⁺ represents He₂(a³Σ_u⁺). O₂(a) represents O₂(a¹Δ_g); O₂(b) represents O₂(b¹Σ_g⁺); O₂(ν) represents the vibrational excited states of O₂ (ν = 1–4). M represents the background gases helium and oxygen. ^{b)}Rate coefficients have units of cm³ · s⁻¹ for two-body reactions and cm⁶ · s⁻¹ for three-body reactions; T_e has units eV; T_g has units K. f(T_e) indicates that the rate coefficient is obtained using the cross section from the indicated reference. ^{c)}S represents main reaction in the whole range of oxygen concentration. S1: main reactions in RG1; S2: main reactions in RG2; S3: main reactions in RG3. ^{d)}Cross-section estimated by shifting the ground state cross section by the excitation threshold. ^{e)}Superelastic cross section calculated using detailed balance. ^{f)}Estimated same as O₂. ^{g)}Estimated same as O. ^{h)}Estimated same as He*.

dissipated as they transit the sheath is much higher (of the order of the actual sheath potential, ≈100 V in this study). In atmospheric pressure plasmas, this energy ends up heating the background gas via ion-neutral collisions in the sheath, rather than reaching the walls as it is the case in low-pressure plasmas.

The foremost purpose of this paper is to identify the main species and chemical reactions in cold atmospheric-pressure He + O₂ plasmas for various oxygen concentrations. Due to the strong dependence of the discharge characteristics on the oxygen concentration, three regimes need to be considered:

- (i) Regime 1 (RG1): Discharges containing 1–10 ppm of oxygen. At this low oxygen concentration, helium species dominate the discharge and the discharge is clearly electropositive.
- (ii) Regime 2 (RG2): Discharges containing 10–5 000 ppm of oxygen. In this regime, oxygen-derived species dominate over helium species, and the discharge becomes increasingly electronegative.
- (iii) Regime 3 (RG3): Discharges containing 0.5–10% of oxygen. In this regime, species originated from helium are negligible, and the discharge is electronegative.

A sensitivity study is performed to select the main species and reactions in each regime. The criterion used is the same as the one detailed in ref.^[22] In brief, once the simulation has reached steady state, only the species whose

density is larger than a threshold value are deemed important. The threshold value is chosen to be 5% of the total density of positive ions (or negative charged species). It is noted, however, that some intermediate species are included in the simplified models despite not reaching the threshold density because they contribute significantly to the particle balance of more abundant species. This is the case, for example, of He⁺. He⁺ density is typically less than the threshold value, but it contributes importantly to the formation of He₂⁺ via $He^+ + 2He \rightarrow He_2^+ + He$ (reaction R142 in Table 2). Since He₂⁺ is the main ion in RG1, He⁺ is also incorporated in the simplified model. The main species identified for each of the three regimes (RG1, RG2 and RG3) are listed in Table 1. Once the main species have been identified, main reactions need to be selected next. As in ref.^[22] this is done by choosing the reactions whose absolute and/or relative contribution to the particle balance of each main species in the plasma is above a certain threshold (5% again). The list of main reactions for the simplified models can be found in Table 2.

Main Species as a Function of the Oxygen Concentration

The steady state composition of He + O₂ plasmas as a function of the oxygen concentration is captured in Figure 2. Figure 2a–d show the density of positive ions, negatively charged species, metastables, and other neutral

Table 3. Wall reactions.

Surface reactions	Probability	Ref.
$He^* + Wall \rightarrow He$	1.00	[18]
$He_2^* + Wall \rightarrow 2He$	1.00	[18]
$O + Wall \rightarrow \frac{1}{2}O_2$	0.02	[18]
$O(^1D) + Wall \rightarrow O$	1.00	[18]
$O(^1S) + Wall \rightarrow O$	1.00	[18]
$O_2(a) + Wall \rightarrow O_2$	0.0004	[83]
$O_2(b) + Wall \rightarrow O_2$	0.02	[18]
$O_2(v) + Wall \rightarrow O_2$	0.2	[18]
$X^+ + Wall \rightarrow neutrals$	1.00	[18]

^{a)} X^+ represents any positive ion.

species, respectively. The figures clearly indicate that the main species depend on the oxygen concentration, and most species undergo density variations of orders of magnitude. Since the data is obtained at constant input power, an increase in density reflects a more efficient generation of that particular species, whereas a decrease in density indicates a decrease in generation efficiency. Figure 2a presents the density of positive ions in the

plasma. As observed in other atmospheric pressure helium discharges,^[35,36] helium dimer ions (He_2^+) are more abundant than helium ions (He^+). Nevertheless, even at oxygen concentrations of just 1 ppm, O_2^+ is the dominant ion. Given the large energy of helium and helium dimer metastables ($\epsilon \approx 19.8$ eV and 18.4 eV, respectively), Penning ionization (R205 and R211) is an important process in He + O_2 discharges and leads to the larger density of oxygen ions. Similar results have been observed in He + N_2 ^[37] and He + H_2O ^[22] discharges. As the oxygen concentration increases, the density of helium ions decreases sharply, while the density of O_4^+ increases rapidly. In fact, the model predicts that O_4^+ becomes the dominant positive ion at high oxygen concentration (regime RG3). A similar trend was observed in atmospheric pressure He + N_2 discharges, where N_4^+ was found to be more abundant than N_2^+ at nitrogen concentrations above a few hundred ppm^[42] and in atmospheric pressure He + H_2O discharges where charged water clusters were more abundant than H_2O^+ .^[22,38] It is noted that larger ions (e.g. O_6^+) are not considered in the current model due to lack of reliable data. Regarding negative ions (Figure 2b), O^- is the dominant one at low oxygen concentration, and O_3^- becomes dominant at $[O_2] > 2000$ ppm as a result of three body collisions (R164). This trend contrasts with that observed in low pressure oxygen plasmas where O_3^- is not

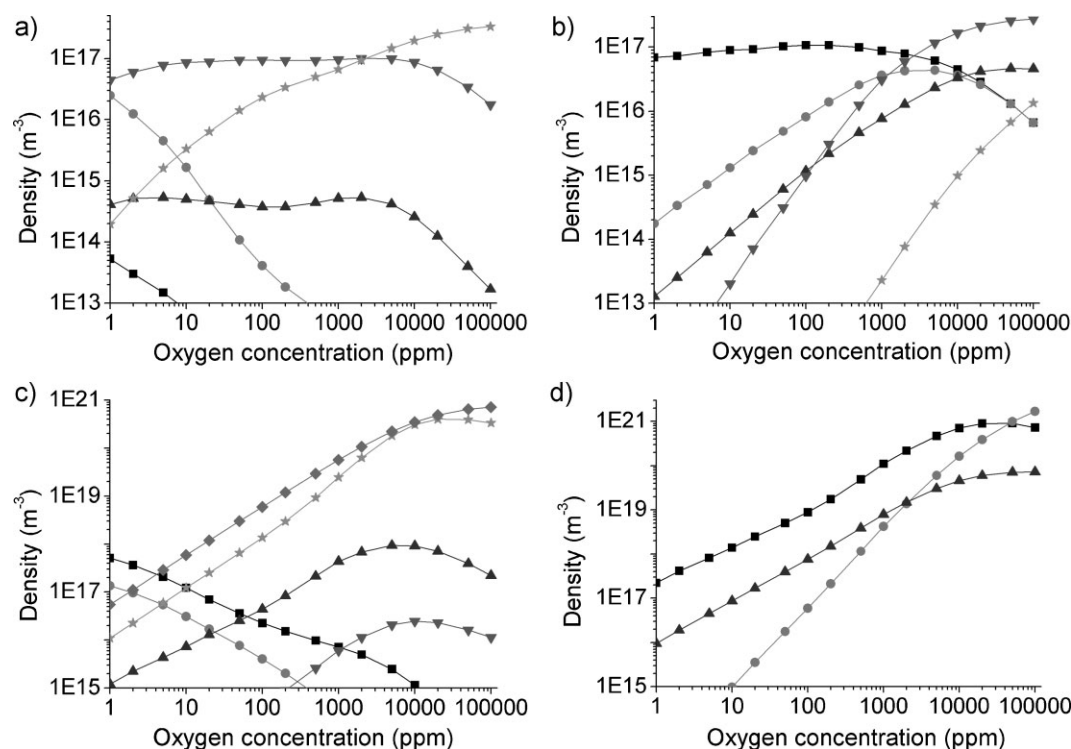


Figure 2. Density of a) positive ions: \blacksquare : He^+ ; \bullet : He_2^+ ; \blacktriangle : O^+ ; \blacktriangledown : O_2^+ ; \star : O_4^+ ; b) negative charged species: \blacksquare : e^- ; \bullet : O^- ; \blacktriangle : O_2^- ; \blacktriangledown : O_3^- ; \star : O_4^- ; c) metastables: \blacksquare : He^* ; \bullet : He_2^* ; \blacktriangle : $O(^1D)$; \blacktriangledown : $O(^1S)$; \star : $O_2(b)$; \blacklozenge : $O_2(a)$; d) other neutral species: \blacksquare : O ; \bullet : O_3 ; \blacktriangle : $O_2(v)$.

abundant.^[39,40] Figure 2b also indicates that the discharge becomes electronegative (i.e. density of negative ions > density of electrons) for oxygen concentrations above $\approx 0.2\%$ and that at that point the electron density starts to decrease with increasing the oxygen concentration. Since at high oxygen concentrations, the discharge is dominated by oxygen species, this trend is similar to that of pure oxygen plasmas.^[44]

The density distribution of excited neutral species in the plasma is shown in Figure 2c. Atomic and dimer helium metastables are the most abundant excited species at low oxygen concentration ($[O_2] < 10$ ppm), while atomic and molecular metastable oxygen are dominant at higher oxygen concentration. This trend is the result of the increasing loss of helium excited species due to Penning processes, the consequent decrease in electron temperature, and the increasing presence of oxygen in the discharge. The predicted density of $O_2(a)$ at high oxygen concentration is in agreement with recent experimental observations in an atmospheric-pressure He + O_2 discharge.^[41] It is noted that the density of helium dimer metastables is lower than that of atomic helium metastables. This is opposite to the results obtained in other fluid models of helium atmospheric pressure discharges^[40,41] and it is attributed to the zero dimensionality of the global model. Since global models average over sheath and bulk, the average electron temperature in the plasma is higher than the bulk electron temperature in fluid models, enhancing the production of He^* over He_2^* . Figure 2c also indicates that excited atomic oxygen species $O(^1D)$ and $O(^1S)$ reach a maximum density when the oxygen concentration is $\approx 0.5\%$. Although atomic oxygen metastables are not easily measured experimentally, this trend of O^* species is qualitatively in agreement with experimental observation of the optical emission intensity at 777nm from $O(^5P)$.^[42,43] Figure 2d presents the density distribution of other neutral species, namely, atomic oxygen, O_3 and vibrational excited O_2 . The O density reaches its maximum at $[O_2] \approx 2\%$, which is in qualitative agreement with other modelling and experimental observations.^[21,44,45] The existence of a maximum is attributed mainly to the decrease in electron density, and the increasing loss of atomic O via O_3 formation (see discussion in section Analysis of physicochemical processes in He + O_2 plasmas). It is noted that most He + O_2 based plasma applications use oxygen concentrations in the range of 0.5 – 3%,^[46] which correspond to the region where atomic oxygen species reach their maximum concentration: O^* 's peak at $[O_2] \approx 0.5\%$ and ground state O at $\approx 2\%$. On the contrary, the density of O_3 continues to grow exponentially with increasing O_2 , becoming more abundant than atomic oxygen when $[O_2] > 2\%$. Although vibrational excitation of molecular oxygen requires low energy, the density of $O_2(v)$ is found to be more than one order of magnitude lower than that of atomic oxygen, and this is attributed to the high

collisional quenching of $O_2(v)$ (R246), and the relatively high electron temperature predicted in the model (see discussion in section Analysis of physicochemical processes in He + O_2 plasmas).

Simplified Models, Their Accuracy and Robustness

Figure 2 clearly indicates that the plasma composition depends strongly on the oxygen concentration. Most plasma species undergo density variations of orders of magnitude, and as a result, a single simplified model cannot capture accurately the chemistry at play for all oxygen concentrations. Therefore, three regimes are considered here and three simplified models are proposed (see Table 1 and 2). The simplified model 1 (RG1) contains 13 species and 24 reactions, the simplified model 2 (RG2) contains 17 species and 41 reactions, and the simplified model 3 (RG3) contains 15 species and 50 reactions. The chemistry complexity of He + O_2 plasmas is therefore lowered by a factor of 5 to 11 with the simplified models. As an example, Figure 3 shows the densities of the dominant ions as a function of oxygen concentration, using the full model (267 reactions) and the three simplified models. Although Figure 3 (and similar data obtained for all the other relevant species) validates the accuracy of the simplified models, this does not guarantee that the same level of accuracy is achieved with the simplified models under different plasma conditions. Therefore, the robustness of the simplified models to changes in the discharge conditions is investigated next. The plasma equilibrium conditions are expected to change as a function of the surface to volume ratio (S_1/V and S_2/V) of the plasma (see Equation 1). Therefore, we assess the robustness of the proposed simplified models by comparing simulation results of the simplified models against the results of the full model for

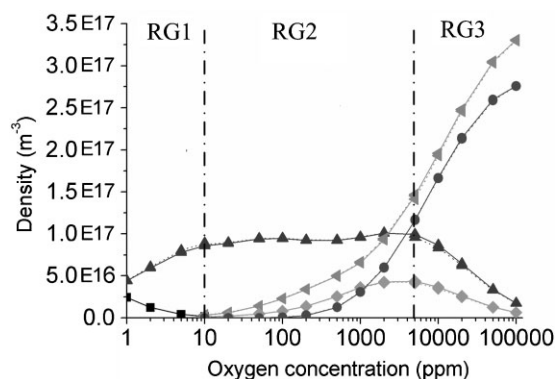


Figure 3. Density of dominant ionic species as a function of the oxygen concentration. \blacksquare : He_2^+ ; \blacktriangle : O_2^+ ; \blacktriangleleft : O_4^+ ; \blacklozenge : O^- ; \bullet : O_3^- . Solid line: full model; dotted line: simplified models.

various gap ($g = V/S_1$) and electrode radius ($r = 2V/S_2$) values (Figure 1). The error introduced by adopting the simplified models is quantified by the root mean squared error (RMSE) with respect to the results obtained with the full model, i.e.:

$$RMSE = \sqrt{\frac{1}{N_m} \sum_{i=1}^{N_m} \left(\frac{n_{is} - n_{if}}{n_{if}} \right)^2} \times 100\% \quad (3)$$

where, N_m denotes the total number of main species in the simplified model, n_{is} the density of i th main species obtained with the simplified model and n_{if} the one obtained with the full model. The RMSE is shown in Figure 4. In Figure 4a–b, the S_1/V and S_2/V ratios vary by a factor of 4, exploring the typical dimensions of experimental cold atmospheric-pressure plasmas in a plane-to-plane configuration. The RMSE is less than 20% for every case, indicating that the simplified models are capable of capturing the main chemical processes despite changes in the plasma source geometry.

According to Equation 2, the input power density (P_{in}/V) affects the electron effective temperature and thereby the source terms in the particle balance equation (Equation 1). For a He + O₂ RF glow discharge, the input power used in

experiments is typically $20\text{--}70 \text{ W} \cdot \text{cm}^{-3}$,^[23] so in this study we assess the validity of the simplified models by simulating discharges with 20, 40, and $80 \text{ W} \cdot \text{cm}^{-3}$. The results are shown in Figure 4c and again, the RMSE is found to be less than 20% for a four-fold change in input power. In addition, the particle balance also depends on the gas temperature and the gas flow rate. In cold atmospheric-pressure plasmas, the gas temperature is typically kept near room temperature. In particular, for applications in plasma medicine, the gas temperature often remains below 40°C .^[1] A quantification of the error introduced by the simplified models when the gas temperature is changed from 300 K to 600 K is shown in Figure 4d. Once more the RMSE is found to be less than 20%.

Finally, the influence of the gas flow in the accuracy of the simplified models is assessed by varying the flow rate from 0 to 1 slm. In this range, the gas flow rate is found to have negligible impact (figure not shown). It is noted that the gas flow is known to influence the uniformity of the discharge and the gas temperature. These dependences, however, are not captured in the global model. It is noted that Figure 4a–d present discontinuities at the boundaries between the three simplified models, i.e. at 10 and 5 000 ppm. This is due to different species being taken into account in each of the simplified models. In addition, it is

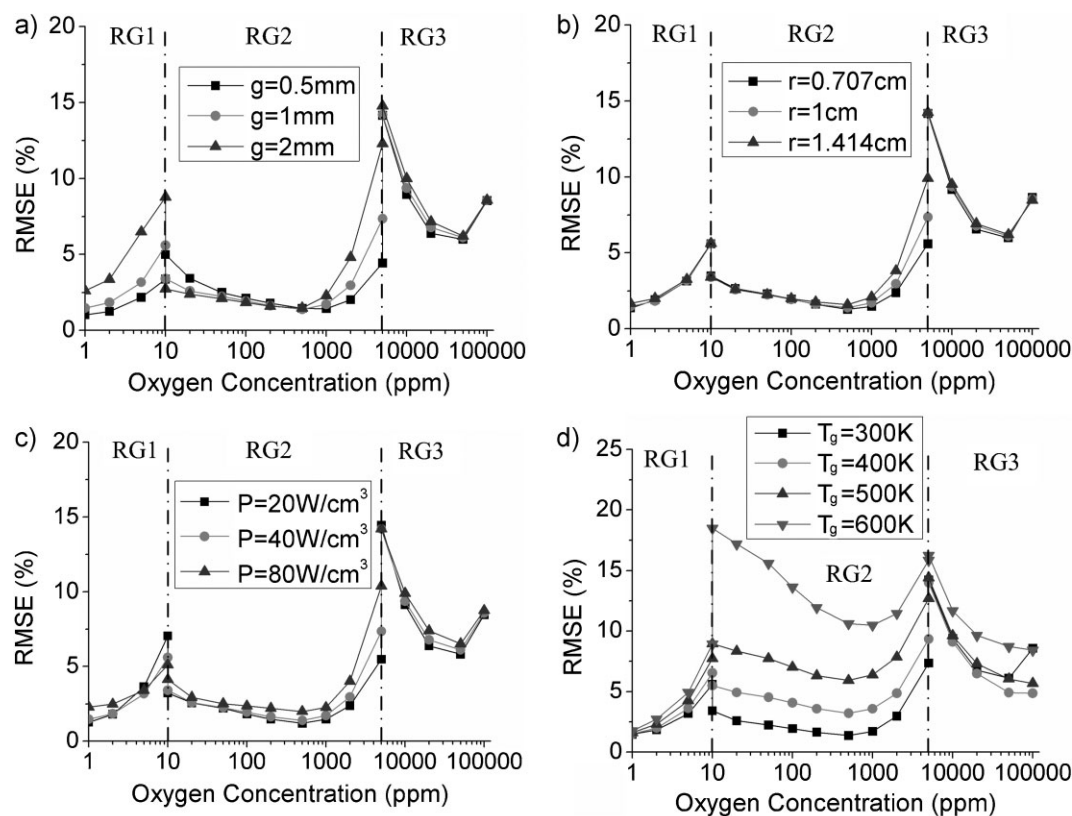


Figure 4. Accuracy of simplified models for plasmas with (a) different gap size, (b) different electrode radius, (c) different input power density, and (d) different gas temperature.

also noted that the RMSE in the high oxygen concentration regime RG3 is higher than that in RG1 and RG2. That is because in RG3 there are a larger number of reactions with relative contributions in the 1–5% range. These reactions are not incorporated in the simplified model, and collectively impact on the final accuracy. Nevertheless, the proposed simplified models capture the physicochemical processes of the discharge with 20% accuracy with respect to the full model.

Analysis of Physicochemical Processes in He + O₂ Plasmas

Simulation results discussed in the remaining of the manuscript are obtained with the full chemistry model. The dependence (at a constant input power of 40 W · cm⁻³) of the electron density and effective electron temperature on the oxygen concentration is shown in Figure 5. The effective electron temperature is on the order of 2.4 eV and the reduced electric field required to sustain the discharge ≈6 Td. These values, however, need to be interpreted with caution, as they result from a zero-dimensional analysis, i.e. they represent a weighted average of the temperature and field across the discharge. At low oxygen concentration ([O₂] < 200 ppm), the effective electron temperature is found to decrease and the electron density to increase with increasing oxygen content. This is mostly attributed to the increasing contribution of Penning processes (including metastable pooling reactions) to the electron generation (see Figure 6a). Above an oxygen concentration of 200 ppm, however, the trend reverses, i.e. the electron temperature increases and the density decreases with increasing oxygen concentration. In this range, the contribution of Penning ionization decreases due to the reduction of the available helium metastables in the plasma (see Figure 2c). At the same time, as the oxygen concentration increases, so does the electron loss via attachment (R47, R49 and R52

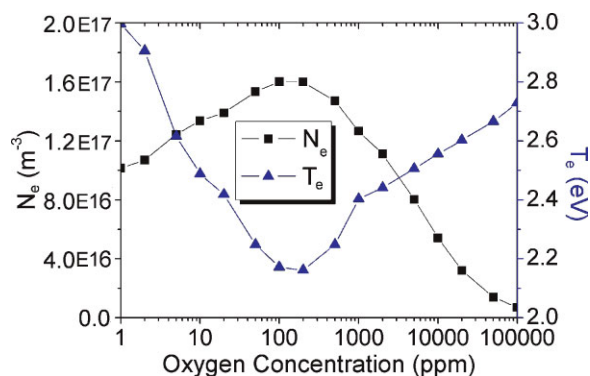


Figure 5. The electron density and electron temperature as a function of oxygen concentration. Results obtained with the full model.

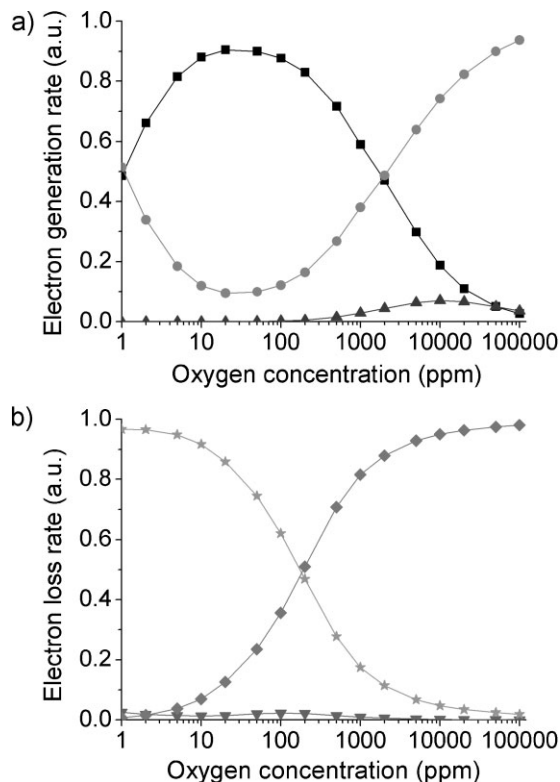


Figure 6. Relative contribution of processes leading to a) generation and b) loss of electrons. —■—: Penning ionization; —●—: Electron impact ionization; —▲—: Collision detachment; —▼—: Dissociative recombination; —★—: Boundary loss; —◆—: Attachment. Results obtained with the full model.

primarily) (see Figure 6b), which ultimately leads to the reduction in electron density and the increase in temperature shown in Figure 5. In order to identify the dominant processes responsible for the generation and loss of electrons, their relative contributions are presented in Figure 6. Figure 6a shows that Penning ionization (R205, R211, etc.) is important, even dominant, for the generation of electrons when the oxygen concentration is less than ≈5 000 ppm. The contribution of electron impact ionization (R3, R4 and R10 primarily) first decreases, reaches a minimum at [O₂] ≈50 ppm, and then increases at higher oxygen concentrations. This trend reflects the changes in electron temperature shown in Figure 5. At low oxygen concentration, electron-impact of He and He* is the dominant electron-impact ionization process, whereas at high oxygen concentration electron-impact of oxygen molecules dominates. Despite the lower concentration of oxygen (< 10%), electron-impact ionization of oxygen molecules can dominate over helium ionization due to the lower ionization threshold of the oxygen molecule (12.6 eV for O₂ vs. 24.6 eV for He). Finally, it is interesting to note that detachment processes (R117, R120, R121, R127 and R131 primarily) contribute significantly at high oxygen concen-

tration. This is an indication of a high density of negative ions at high oxygen concentrations (see Figure 2b). Regarding electron losses, these are dominated at low oxygen concentration by electrons escaping the discharge through the boundaries. As already mentioned, however, electron attachment (R47, R49 and R52 primarily) increases with increasing the oxygen content and in fact it becomes a dominant electron loss mechanism for oxygen concentrations above a few hundred ppm. Electron-ion recombination is found to be negligible for the conditions encountered in typical cold atmospheric pressure discharges. This mechanism, however, could be important in discharges with higher plasma density. Although the electron density starts to drop at oxygen concentrations above ≈ 200 ppm, the degree of ionization continues to increase with increasing oxygen concentration (see Figure 7). This is a combined effect of the lower energy required to ionize oxygen species, and the increasing electron attachment in the discharge. As a result, the electronegativity of the plasma, i.e. the ratio between the number of negative ion and that of electrons, is almost proportional to the oxygen concentration. A similar electronegativity trend has been observed in low pressure Ar + O₂ plasmas.^[28] The model predicts an electronegativity of 1 at an oxygen concentration of $\approx 0.2\%$. The increasing electronegativity affects the electron density, and it translates experimentally in the need for higher voltage to ignite and sustain the plasma.^[23]

Finally, the energy dissipation in the discharge (Figure 8) is discussed here. Collisions (second term in the right hand side of equation 2) consume more energy than the boundaries (last term in the right hand of equation 2), indicating that more power is coupled to the electrons in the bulk plasma than to ions in the sheaths. This is in agreement with other modeling works of atmospheric pressure plasmas.^[47] It is interesting to note, however, that, while losses via elastic collisions dominate at low oxygen concentration, losses via inelastic collisions become dominant at high oxygen concentration. This trend reflects the

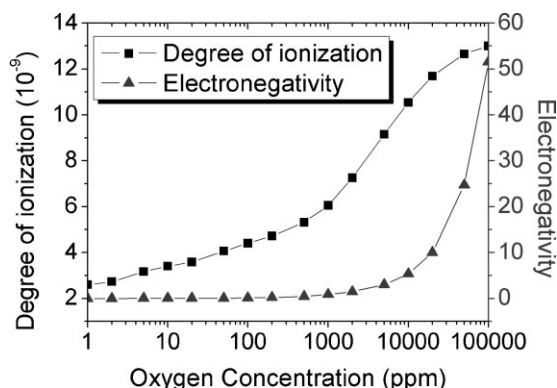


Figure 7. Degree of ionization and electronegativity of a He + O₂ plasma as a function of the oxygen concentration. Results obtained with the full model.

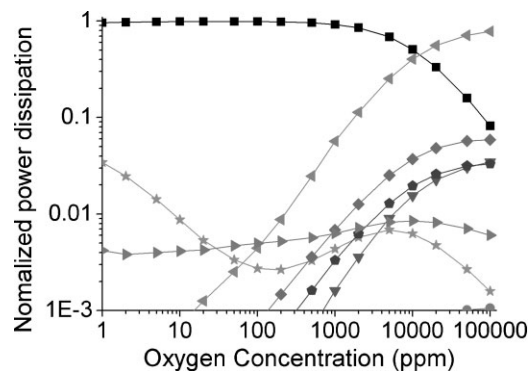


Figure 8. Power deposition as a function of the oxygen concentration. —■—: He elastic collisions; —●—: O₂ elastic collisions; —▲—: He ionization (includes stepwise ionization); —▼—: O₂ ionization (includes stepwise ionization); —★—: He excitation; —◆—: O₂ electronic excitation; —◇—: O₂ vibrational excitation; —◄—: O₂ dissociation (includes dissociative excitation and dissociative attachment); —◄—: Electrode boundary loss. Results obtained with the full model.

evolution of the electron temperature, the increasing significance of electron attachment and the lower (8-fold) energy loss in elastic collisions with O₂ molecules than with He atoms. In particular, at high oxygen concentration, the electron energy is channeled into O₂ dissociation. In addition, the increase in oxygen content introduces another route of energy dissipation: vibrational excitation. Although O₂(*v*) is often neglected in numerical studies, significant amount of energy can be dissipated via vibrational excitation due to the low energy required to excite the oxygen molecules. It can be seen that in RG3 more than 1% of the input power is consumed by vibrational excitation. This is likely to be an underestimation, since as mentioned earlier, the electron temperature in the global model (Figure 5) is likely to be larger than that encountered in the bulk plasma. With a lower electron temperature in the bulk, the fraction of energy consumption in vibrational excitation would be higher,^[15] and therefore vibrational excitation should not be neglected when the oxygen concentration is high.

Source of Reactive Oxygen Species (ROS)

He + O₂ plasmas are a good source of reactive oxygen species (ROS) and in this section we analyze the main ROS produced in these discharges. One of the most abundant ROS produced in He + O₂ plasmas is ground state atomic oxygen, and its generation has received a lot of attention recently because O is believed to be an important antibacterial agent.^[48] The oxidation potential of atomic O is even higher than that of ozone (2.42 V for O vs. 2.07 V for O₃) and second only to fluorine (3.03 V) and hydroxyl

radicals (2.8 V). The relative contribution of the processes leading to the gain/loss of ground state atomic oxygen is illustrated in Figure 9. Figure 9a indicates that more than half of the atomic oxygen is directly generated by electron impact reactions, including dissociation (R25), dissociative excitation (R26 and R27) and dissociative attachment (R47). Nevertheless, about a 40% of the ground state atomic oxygen is generated via collisional quenching of oxygen metastables. The cross section for dissociative excitation of O_2 to form $O(^1D)$ is large (R26),^[49] and as a result quenching of $O(^1D)$ (R215, R216, R217 and R220) is a significant process for generating ground state oxygen. At low oxygen concentration, the quenching is mainly caused by helium atoms (R120) and, as the oxygen concentration increases, quenching by O_2 molecules becomes increasingly important (R215-217). At high oxygen concentrations, the quenching of $O_2(b)$ by O_3 (R241) molecules also contributes to the generation of ground state atoms. Similar trends have been observed in ref.^[20] The processes leading to the destruction of ground state atomic oxygen are shown in Figure 9b. At low oxygen concentration, the loss of atomic oxygen is mainly due to sidewise diffusion. Therefore, an enclosed chamber and low flow rates are beneficial to

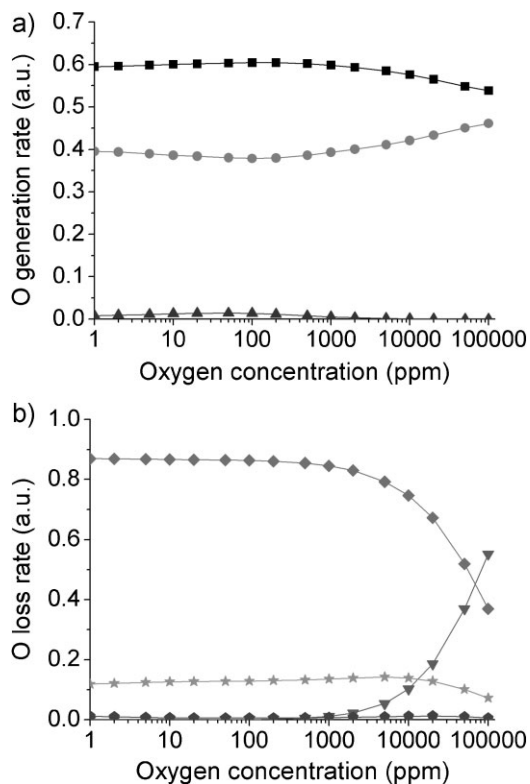


Figure 9. Processes contributing to a) generation and b) loss of ground state atomic oxygen. —■—: Electron impact reactions; —●—: Metastable quenching; —▲—: Other generation processes; —▼—: Formation of O_3 due to three-body reactions; —★—: Electrode loss; —◆—: Sidewise advection; —◇—: Other reduction processes. Results obtained with the full model.

increase the ground state oxygen concentration. In addition, about 10% of the ground state atomic oxygen is consumed by surface reactions (see Table 3). It is known that different material and surface conditions have different surface reaction probabilities, and therefore the yield of atomic oxygen can also be improved by selecting a non-catalyst electrode with smooth surface. At oxygen concentrations above ≈ 1000 ppm, the formation of O_3 via three-body reactions (R258 and R259 primarily) becomes an increasingly important mechanism for the loss of ground state atomic oxygen. Besides ground state atomic oxygen, He + O_2 plasmas produce other reactive oxygen species that are relevant for biomedical applications. Figure 10 presents the densities of ground state atomic oxygen, excited atomic and molecular oxygen, and ozone as a function of the oxygen concentration in the feed gas. The maximum concentration of ROS is found to be at $\approx 2\%$ of oxygen concentration, which agrees qualitatively with other simulation results and experimental observations.^[21,49,50] The ozone density is found to be orders of magnitude smaller than the density of ground state atomic oxygen, although it increases with increasing oxygen concentration (Figure 10). As observed in reference,^[1] the ozone density reaches $\approx 10\%$ the density of ground state atomic oxygen at $[O_2] \approx 0.5\%$. These values assume a well control environment. In many practical scenarios, however, the plasmas are often operated in open air ($[O_2]_{\text{air}} \approx 21\%$), and therefore the ozone generation may be strongly favored in the afterglow. The density of excited atomic oxygen O^* is ≈ 2 orders of magnitude lower than the density of ground state O and it peaks at an oxygen concentration of $\approx 0.5\%$, in qualitative agreement with experimental observations.^[47,48] On the other hand, the density of excited molecular oxygen O_2^* is comparable to that of O. It is noted that these excited species, although less abundant than O, can be more efficient in reacting with biological substrates as they carry additional energy that can assist in breaking existing chemical bonds. Although overlooked in many

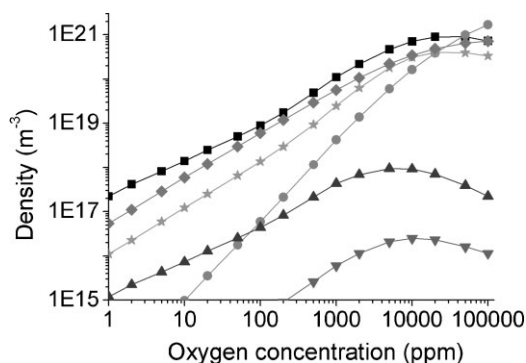


Figure 10. Density of reactive oxygen species. —■—: O; —●—: O_3 ; —▲—: $O(^1D)$; —▼—: $O(^1S)$; —★—: $O_2(b)$; —◆—: $O_2(a)$. Results obtained with the full model.

plasma studies, these species are well-known in the free radical biology community.^[50] In addition to neutral species, some negatively charged ions are also well-known oxidizers in biological systems (e.g. super-oxide O_2^-).^[55] In RF plasmas, however, the ambipolar potential is expected to confine negative ions and therefore these species would probably play a minor role. Nonetheless, in pulsed discharges their flux of negative ions should be larger and then O^- , O_2^- , O_3^- and O_4^- should also be taken into account. Experimentally, the emission at 777 nm from $O(^5P)$ and 845 nm from $O(^3P)$ are usually used to infer the atomic oxygen content in the discharge.^[47,48,51] However, it is noted that in atmospheric pressure He + O_2 plasmas the density evolution of O^* and O may not be the same. As shown in Figure 10, the evolution of O^* and O as a function of the oxygen content are significantly different when the oxygen concentration is above 1 000 ppm (typical regime of operation). This is because the quenching rate of O^* by O_2 is several orders of magnitude higher than that by He and therefore at high oxygen concentrations ($> 5\ 000$ ppm) the density of O^* starts to decrease, while the density of O still increases. Although $O(^5P)$ and $O(^3P)$ are not explicitly considered in the global model, a similar trend to that of O^* should be expected as their quenching rate by O_2 molecules is two orders of magnitude larger than the quenching rate by He atoms ($\approx 7 \times 10^{-10} s^{-1}$ by O_2 vs. $7 \times 10^{-12} s^{-1}$ by He).^[52,53]

Finally, it is recognized that only species crossing the sheaths will react with a biological sample and therefore we present the main fluxes in Figure 11. Given the neutral nature of the reactive oxygen species discussed above, their density in the discharge and their flux to the electrodes follow the same trend. This is not the case, however, for all charged species. Superoxide (O_2^-) and other negatively charged species are confined in the bulk plasma by the

ambipolar potential and their flux to the walls is therefore negligible. As shown in Figure 11, the flux of helium metastables rapidly reduces with increasing the oxygen concentration and the flux of charged species (note that the total flux of positively charged species is equal to the flux of electrons) is also much smaller than the flux of neutral reactive oxygen species.

Conclusion

A comprehensive model of the chemistry of cold atmospheric pressure He + O_2 plasmas that includes 21 species and 267 chemical reactions is presented. By detailed analysis of the simulation results, 3 simplified models are proposed to model these plasmas when the oxygen concentration ranges between 1 ppm and 10%. The simplified models reduce the number of reactions by a factor of 5–11, while capturing the main physicochemical processes with an accuracy better than 20%. The robustness of the simplified models against changes in discharge geometry, input power and gas temperature has also been assessed and it is found that the proposed models remain accurate in a wide range of relevant experimental conditions. Therefore, the simplified models provide a valuable subset of reactions that can be incorporated in more complex simulations where computational cost prevents the use of very large chemistry models.

As the oxygen concentration increases from 1 ppm to 10%, the He + O_2 plasma undergoes a mode transition. At low oxygen concentrations, the electron density decreases and the density increases due to Penning ionization of oxygen molecules. For oxygen concentrations above 200 ppm, however, this trend reverses and the electron temperature starts to increase and the density to decrease with increasing oxygen concentration. This is attributed to the growing role of electron attachment that leads to the formation of an electronegative discharge for $[O_2] > \approx 0.2\%$. It is also noted that, as the oxygen concentration increases, the main electron energy dissipation shifts from elastic collisions with He atoms to dissociative excitation and attachment of O_2 . He + O_2 plasmas are shown to be a good source of reactive oxygen species (ROS). Although major attention has been devoted to ground state atomic oxygen, it is shown that He + O_2 plasmas create a cocktail of ROS that also incorporates large amounts of singlet oxygen and ozone, free radicals well known in biology.

Diffusion/advection governs the loss of many of the ROS, and therefore operation in an enclosed chamber with low flow rates and the use of electrodes with low surface reaction probability are suggested as routes to increase the density of these species in the plasma. It is also shown that the emission intensity at 777 nm and 845 nm commonly used experimentally to infer the concentration of ground

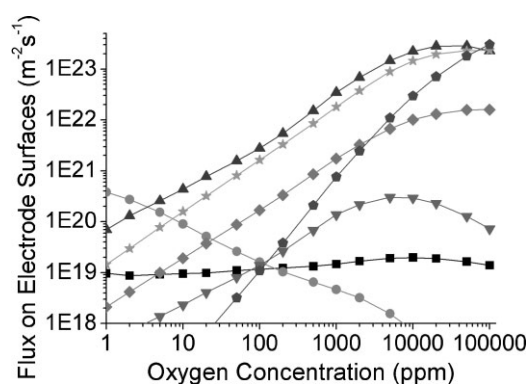


Figure 11. Flux of different species on the electrode surfaces as a function of oxygen concentration. —■—: Electron (or positive ions); —●—: Helium metastables; —▲—: Ground state O; —▼—: O^* ($O(^5D)$ and $O(^3S)$); —★—: Electronic excited O_2 ($O_2(a)$ and $O_2(b)$); —◆—: Vibrational excited O_2 ; —◊—: O_3 . Results obtained with the full model.

state O is not precise, as O* and O present different evolutions at oxygen concentrations above 1 000 ppm.

Acknowledgements: The authors would like to thank Prof. Yuantao Zhang (Shandong University, China) for fruitful discussions related to this work. This work was supported by the National Natural Science Foundation of China (No.50525722 and 50907353), the State Key Laboratory of Electrical Insulation and Power Equipment (No. EIPE10310) and the Engineering Physical Science Research Council (UK).

Received: April 10, 2010; Revised: June 4, 2010; Accepted: July 16, 2010; DOI: 10.1002/ppap.201000049

Keywords: atmospheric pressure glow discharges (APGD); biomedical; cold plasma; modeling; oxygen

- [1] M. G. Kong, G. Kroesen, G. Morfill, T. Nosenko, T. Shimizu, J. van Dijk, J. L. Zimmermann, *New J. Phys.* **2009**, *11*, 115012.
- [2] G. Fridman, G. Friedman, A. Gutsol, A. B. Shekhter, V. N. Vasilets, A. Fridman, *Plasma Processes Polym.* **2008**, *5*, 503.
- [3] F. Iza, G. J. Kim, S. M. Lee, J. K. Lee, J. L. Walsh, Y. T. Zhang, M. G. Kong, *Plasma Processes Polym.* **2008**, *5*, 322.
- [4] R. Hackam, H. Akiyama, *IEEE Trans. Dielectr. Electr. Insul.* **2000**, *7*, 654.
- [5] A. Mfopara, M. J. Kirkpatrick, E. Odic, *Plasma Chem. Plasma Process.* **2009**, *29*, 91.
- [6] M. Laroussi, *IEEE Trans. Plasma Sci.* **2002**, *30*, 1409.
- [7] X. Deng, J. J. Shi, M. G. Kong, *J. Appl. Phys.* **2007**, *101*, 074701.
- [8] A. N. Bhoj, M. J. Kushner, *Plasma Sources Sci. Technol.* **2008**, *17*, 035024.
- [9] T. Suzuki, T. Saburi, R. Tokunami, H. Murata, Y. Fujii, *Thin Solid Films* **2006**, *506–507*, 342.
- [10] P. Bruggeman, C. Leys, *J. Phys. D: Applied Phys.* **2009**, *42*, 053001.
- [11] M. A. Malik, A. Ghaffar, S. A. Malik, *Plasma Sources. Sci. Technol.* **2001**, *10*, 82.
- [12] C. J. Howard, *J. Phys. Chem.* **1979**, *83*, 3.
- [13] M. A. Lieberman, A. J. Lichtenberg, *Principles of Plasma Discharges and Materials Processing*, 2nd Ed., Wiley-VCH, New-York 2005.
- [14] A. Friedman, *Plasma Chemistry*, Cambridge University Press, Cambridge 2008.
- [15] A. A. Ionin, I. V. Kochetov, A. P. Napartovich, N. N. Yuryshv, *J. Phys. D: Appl. Phys.* **2007**, *40*, R25.
- [16] A. Hicks, S. Norberg, P. Shawcross, W. R. Lempert, J. W. Rich, I. V. Adamovich, *J. Phys. D: Appl. Phys.* **2005**, *38*, 3812.
- [17] L. Lee, M. A. Lieberman, *J. Vac. Sci. Technol. A* **1995**, *32*, 368.
- [18] D. S. Stafford, M. J. Kushner, *J. Appl. Phys.* **2004**, *96*, 2451.
- [19] G. Y. Park, H. W. Lee, G. Kim, J. K. Lee, *Plasma Processes Polym.* **2008**, *5*, 569.
- [20] G. Y. Park, Y. J. Hong, H. W. Lee, J. Y. Sim, J. K. Lee, *Plasma Processes Polym.* **2010**, *7*, 281.
- [21] S. J. Kim, M. A. Lieberman, A. J. Lichtenberg, J. T. Gunmundsson, *J. Vac. Sci. Technol. A* **2006**, *24*, 2025.
- [22] D. X. Liu, P. Bruggeman, F. Iza, M. Z. Rong, M. G. Kong, *Plasma Sources Sci. Technol.* **2010**, *19*, 025018.
- [23] D. Liu, F. Iza, M. G. Kong, *IEEE Trans. Plasma Sci.* **2008**, *36*, 952.
- [24] T. Kimura, A. J. Lichtenberg, M. A. Lieberman, *Plasma Sources Sci. Technol.* **2001**, *10*, 430.
- [25] R. Deloche, P. Monchicourt, M. Cheret, F. Lambert, *Phys. Rev. A* **1976**, *13*, 1140.
- [26] T. Martens, A. Bogaerts, W. Brok, J. V. Dijk, *Anal. Bioanal. Chem.* **2007**, *388*, 1583.
- [27] F. J. Gordillo-Vazquez, *J. Phys. D: Appl. Phys.* **2008**, *41*, 234016.
- [28] J. T. Gudmundsson, E. G. Thorsteinsson, *Plasma Sources Sci. Technol.* **2007**, *16*, 399.
- [29] K. R. Stalder, R. J. Vidmar, G. Nersisyan, W. G. Graham, *J. Appl. Phys.* **2006**, *99*, 093301.
- [30] M. J. Kushner, *Bull. Am. Phys. Soc.* **1999**, *44*, 63.
- [31] I. A. Kossyi, A. Y. Kostinsky, A. A. Matveyev, V. P. Silakov, *Plasma Sources Sci. Technol.* **1992**, *1*, 207.
- [32] G. J. M. Hagelaar, L. C. Pitchford, *Plasma Sources Sci. Technol.* **2005**, *14*, 722.
- [33] D. D. Monahan, M. M. Turner, *Plasma Sources Sci. Technol.* **2008**, *17*, 045003.
- [34] S. S. Yang, S. M. Lee, F. Iza, J. K. Lee, *J. Phys. D: Appl. Phys.* **2006**, *39*, 2775.
- [35] D. W. Liu, F. Iza, M. G. Kong, *Plasma Process. Polymers.* **2009**, *6*, 446.
- [36] F. Iza, J. K. Lee, *J. Vac. Sci. Technol. A* **2006**, *24*, 1366.
- [37] F. Iza, J. K. Lee, M. G. Kong, *Phys. Rev. Lett.* **2007**, *99*, 75004.
- [38] J. Choi, F. Iza, J. K. Lee, C. M. Ryu, *IEEE Trans. Plasma Sci.* **2007**, *35*, 1274.
- [39] G. J. Kim, F. Iza, J. K. Lee, *J. Phys. D: Appl. Phys.* **2006**, *39*, 4386.
- [40] Q. Wang, D. J. Economou, V. M. Donnelly, *J. Appl. Phys.* **2006**, *100*, 023301.
- [41] J. J. Shi, M. G. Kong, *J. Appl. Phys.* **2005**, *97*, 023306.
- [42] T. Martens, A. Bogaerts, W. J. M. Brok, J. V. Dijk, *Appl. Phys. Lett.* **2008**, *92*, 041504.
- [43] P. Bruggeman, F. Iza, D. Lauwers, Y. Aranda, Gonzalvo, *J. Phys. D: App. Phys.* **2010**, *43*, 012003.
- [44] E. Stoffels, W. W. Stoffels, D. Vender, M. Kando, G. M. W. Kroesen, F. J. Hoog, *Phys. Rev. E* **1995**, *51*, 2425.
- [45] J. T. Gudmundsson, I. G. Kouznetsov, K. K. Patel, M. A. Lieberman, *J. Phys. D: Appl. Phys.* **2001**, *34*, 1100.
- [46] J. Santos Sousa, G. Bauville, B. Lacour, V. Puech, M. Touzeau, L. C. Pitchford, *Appl. Phys. Lett.* **2008**, *93*, 011502.
- [47] V. Leveille, S. Coulombe, *Plasma Process. Polym.* **2006**, *3*, 587.
- [48] B. Wang, W. Zhu, Y. Pu, *Plasma Sci. Technol.* **2005**, *7*, 3045.
- [49] N. Knake, K. Niemi, S. Reuter, V. Schulz-von der Gathen, J. Winter, *Appl. Phys. Lett.* **2008**, *93*, 131503.
- [50] D. Ellerweg, J. Benedikt, A. von Keudell, N. Knake, V. Schulz-von der Gathen, *New J. Phys.* **2010**, *12*, 013021.
- [51] J. Park, I. Henins, H. W. Herrmann, G. S. Selwyn, J. Y. Jeong, R. F. Hicks, D. Shim, C. S. Chang, *Appl. Phys. Lett.* **2000**, *76*, 288.
- [52] T. Farouk, B. Farouk, A. Gutsol, A. Fridman, *Plasma Sources Sci. Technol.* **2008**, *17*, 035015.
- [53] S. Moreau, M. Moisan, M. Tabrizian, J. Barbeau, J. Pelletier, A. Ricard, L. H. Yahia, *J. Appl. Phys.* **2000**, *88*, 1166.
- [54] B. Eliasson, U. Kogelschatz, *Basic data for modeling of electrical discharge in gases: Oxygen*, Report KLR-86-11C, Brown Boveri Forschungszentrum CH-5405 Baden 1986.
- [55] W. A. Pryor, K. N. Houk, C. S. Foote, J. M. Fukuto, L. J. Ignarro, G. L. Squadrito, K. J. Davies, *Am. J. Physiol. Regul. Integr. Comp. Physiol.* **2006**, *291*, R491.
- [56] M. A. Khan, A. M. Al-Jalal, *Appl. Phys. Lett.* **2006**, *89*, 171501.
- [57] K. Niemi, V. Schulz-von der Gathen, H. F. Dobelev, *J. Phys. D: Appl. Phys.* **2001**, *34*, 2330.

- [58] B. F. Gordiets, C. M. Ferreira, V. L. Guerra, J. M. A. H. Loureiro, J. Nahorny, D. Pagnon, M. Touzeau, M. Vialle, *IEEE Trans. Plasma Sci.* **1995**, *23*, 750.
- [59] BOLSIG+ software version 1.1., 2008, <http://www.siglokinema.com/technical.htm> (accessed April, 2010).
- [60] Y. Itikawa, A. Ichimura, K. Onda, K. Sakimoto, K. Takayanagi, Y. Hatano, M. Hayashi, M. Nishimura, S. Tsurubuchi, *J. Phys. Chem. Ref. Data* **1989**, *18*, 23.
- [61] R. K. Janev, W. D. Langer, J. K. Evans, D. E. Post, *Elementary processes in hydrogen-helium plasmas: Cross Sections and Reaction Rate Coefficients*, Springer, Berlin 1987.
- [62] S. Rauf, M. J. Kushner, *J. Appl. Phys.* **1999**, *85*, 3460.
- [63] R. R. Laher, F. R. Gilmore, *J. Phys. Chem. Ref. Data* **1990**, *19*, 277.
- [64] G. C. Tisone, L. M. Branscomb, *Phys. Rev.* **1968**, *170*, 169.
- [65] J. W. McConkey, C. P. Malone, P. V. Johnson, C. Winstead, V. McKoy, I. Kanik, *Phys. Rep.* **2008**, *466*, 1.
- [66] R. I. Hall, S. Trajmar, *J. Phys. B: Atom. Molec. Phys.* **1975**, *8*, L293.
- [67] Y. Itikawa, A. Ichimura, *J. Phys. Chem. Ref. Data* **1990**, *19*, 637.
- [68] P. D. Burrow, *J. Chem. Phys.* **1973**, *59*, 4922.
- [69] S. L. Akhmanov, K. S. Klopovskiy, A. P. Osipov, *Manuscript 5472-83 deposited in VINITI*, Moscow (in Russian) 1983.
- [70] Y. B. Golubovskii, V. A. Maiorov, J. Behnke, J. F. Behnke, *J. Phys. D: Appl. Phys.* **2003**, *36*, 39.
- [71] M. J. Wynn, J. D. Martin, *J. Chem. Phys.* **1970**, *52*, 191.
- [72] R. J. Vidmar, K. R. Stalder, *Computations of the power to sustain plasma in air with relevance to aerospace technology*. Final report prepared for Air Force Office of Scientific Research. Report No.: AFRLSRARRE040123. Contract No: F49620-01-1-0414. Feb. 20, 2004.
- [73] S. D. T. Axford, A. N. Hayhurst, *Proc. Math. Phys. Eng. Sci.* **1996**, *452*, 1007.
- [74] O. Eichwald, M. Yousfi, A. Hennad, O. Lamrous, *J. Appl. Phys.* **1997**, *82*, 4781.
- [75] R. P. Cardoso, T. Belmonte, G. Henrion, N. Sadeghi, *J. Phys. D: Appl. Phys.* **2006**, *39*, 4178.
- [76] A. Good, *Chem. Rev.* **1975**, *75*, 561.
- [77] N. G. Adams, D. K. Bohme, D. B. Dunkin, F. C. Fehsenfeld, E. E. Ferguson, *J. Chem. Phys.* **1970**, *52*, 3133.
- [78] R. Atkinson, D. L. Baulch, R. A. Cox, R. F. Hampson, Jr, J. A. Kerr, M. J. Rossi, J. Troe, *J. Phys. Chem. Ref. Data* **1997**, *26*, 521.
- [79] NIST chemical kinetic database, <http://kinetics.nist.gov/kinetics/index.jsp> (accessed April, 2010).
- [80] S. Hadi-Ziane, B. Held, P. Pignolet, *J. Phys. D: Appl. Phys.* **1992**, *25*, 677.
- [81] L. Deng, W. Shi, H. Yang, G. Sha, C. Zhang, *Rev. Sci. Instrum.* **2004**, *75*, 4455.
- [82] E. C. Zipf, *Canadian J. Chem.* **1969**, *47*, 1863.
- [83] Y. V. Savin, L. V. Goryachev, Y. A. Adamenkov, T. V. Rakhimova, Y. A. Mankelevich, N. A. Popov, A. A. Adamenkov, V. V. Egorov, S. P. Ilyin, Y. V. Kolobyanin, E. A. Kudryashov, G. S. Rogozhnikov, B. A. Vyskubenko, *J. Phys. D: Appl. Phys.* **2004**, *37*, 3121.